



JGR Space Physics

RESEARCH ARTICLE

10.1029/2019JA027383

Special Section:

Equatorial Aeronomy: New results from the 15th International Symposium on Equatorial Aeronomy (ISEA-15) and beyond

Key Points:

- The first extended period of FPI measurements of thermospheric dynamics from Northern Africa are presented over 3 years
- Properties of the thermospheric winds are analyzed for both quiet and disturbed conditions during a period of declining solar flux
- A superposed epoch analysis is applied to the stormtime meridional winds to study the occurrence of traveling atmospheric disturbances

Correspondence to:

A. Loutfi,
loutifi.amal@gmail.com

Citation:

Loutfi, A., Bounhir, A., Pitout, F., Benkhaldoun, Z., & Makela, J. J. (2020). Thermospheric neutral winds above the Oukaimeden Observatory: Effects of geomagnetic activity. *Journal of Geophysical Research: Space Physics*, 125, e2019JA027383. <https://doi.org/10.1029/2019JA027383>

Received 10 OCT 2019

Accepted 15 MAY 2020

Accepted article online 10 JUN 2020

Thermospheric Neutral Winds Above the Oukaimeden Observatory: Effects of Geomagnetic Activity

A. Loutfi^{1,2} , A. Bounhir¹, F. Pitout² , Z. Benkhaldoun¹, and J. J. Makela³ 

¹Oukaimeden Observatory, Laboratory of High Energy Physics and Astrophysics, FSSM, Cadi Ayyad University, Marrakech, Morocco, ²IRAP, CNES/CNRS/Toulouse University, Toulouse, France, ³Department of Electrical and Computer Engineering, University of Illinois at Urbana-Champaign, Urbana, IL, USA

Abstract In the context of space weather, we investigate the effect of geomagnetic activity on Earth's thermosphere above the Oukaimeden Observatory in Morocco (geographic coordinates: 31.206°N, 7.866°W; magnetic latitude: 22.77°N) over 3 years from 2014 to 2016. The observatory is equipped with a Fabry-Perot interferometer (FPI) that provides measurements of thermospheric wind speed. In this study 41 disturbed nights (with SYM-H ≤ -50 nT, Kp ≥ 5) were identified and analyzed. We have characterized the meridional and zonal winds variability and dependence on the solar cycle, during both quiet and disturbed conditions. We have classified the storm time meridional neutral winds into three types of variation. The first type is characterized by traveling atmospheric disturbance (TAD)-induced circulation: the first TAD coming from the north and the second TAD being transequatorial, coming from the south. This type of storm with TAD-induced circulation accounts for 59% of the cases. The second type exhibits only slight discrepancies between the disturbed and quiet night flows. These cases account for 33% of the cases. The third type is characterized by the transequatorial wind in whole the night. This last type accounts for 8% of the cases. Finally, we apply a superposed epoch analysis method on the FPI data, and the effect of each phase of the geomagnetic storm on the wind flow and vertical total electron content VTEC has been quantified.

1. Introduction

The Sun is responsible for several magnetic, electrical, and thermal disturbances that affect technological equipment, especially communication satellites, GPS systems, and electrical power grids. During geomagnetic perturbations, the thermospheric neutral winds undergo large and complex dynamics, which can couple into the ionosphere, producing great disturbances in the electric field, the drifts of plasma, and currents from high to equatorial latitudes (Fejer et al., 2016). Understanding this coupling, and its dependencies on the season, location, and magnitude of the disturbance, is a major focus of the space weather community.

Many efforts have been made to study the climatology of thermospheric neutral winds through incoherent scatter radars (ISRs), ground-based ion sondes (Aruliah et al., 1996; Biondi et al., 1999; Buonsanto & Witasse, 1999; Duboin & Lafeuille, 1992; Emmert et al., 2003; Fejer et al., 2002; Fesen et al., 1995; Hagan, 1993; Kawamura et al., 2000; Liu, 2004), Fabry-Perot interferometers (FPIs), and in situ measurements (Biondi et al., 1991; Biondi et al., 1999; Hedin et al., 1994; Hernandez & Roble, 1984, 1995). Theoretical calculations for both general thermospheric circulation (Fuller-Rowell & Rees, 1980; Roble et al., 1988) and under disturbed conditions (Burns et al., 2004; Fejer et al., 2002; Wang et al., 2004) have been reported in the literature. These investigations have contributed greatly to our understanding of the upper thermosphere's responses as a function of time of day, season, latitude, longitude, solar cycle, and geomagnetic activities. However, there still remain lots of unresolved problems, such as the complexities of the spatially and temporally dependent response of the thermosphere to strong external forcing during geomagnetic storms at low geographic and subtropical geomagnetic latitudes.

When the energy of magnetospheric origin is suddenly transferred to the thermosphere at high latitudes, mostly in the form of Joule heating (Knipp et al., 2004), available evidence indicates that a longitudinally extended wavefront propagates away from the source region. This disturbance is often referred to as a large-scale traveling atmospheric disturbance (TAD). They not only transport momentum and energy deposited at high latitudes to the middle- and low-latitude regions of the thermosphere but also transport

momentum and energy from the lower thermosphere into the upper thermosphere. TADs represent one mechanism for globally redistributing energy and momentum within the thermosphere in connection with magnetic storms and substorms and thus are fundamental to our understanding of this aspect of solar-terrestrial coupling. Historically, due to the more widespread availability of remote sensing measurements of the ionosphere, manifestations of TADs in various ionospheric parameters are more commonly observed and referred to as traveling ionospheric disturbances (TIDs) (Sean et al., 2007).

This paper aims to study the thermospheric winds during geomagnetic disturbances above the Oukaimeden Observatory in Morocco (geographic coordinates: 31.206°N, 7.866°W; magnetic latitude: 22.77°N). This work represents the first time such a comprehensive study has been achieved in North Africa. Data used in this study were collected during a declining solar cycle (2014–2016) and are valuable to understand the possible effects of the declining solar cycle on thermospheric winds and geomagnetic storms. In Section 2, we describe the FPI instrument and methods used to produce the estimates of the thermospheric neutral winds. Section 3 provides an analysis of thermospheric winds above the Oukaimeden Observatory during 3 years of observations, both during quiet and disturbed conditions. Along with the presentation of the data, we have proceeded to a comparison of the winds with the HWM model to be described in more detail in Section 2.4. Daily, annual, and seasonal variations of disturbed nights are presented and compared to quiet nights and HWM model results. We also produce a general classification of the thermospheric response to the storms observed during the study period. Then, we present a superposed epoch analysis of the disturbed data that has been achieved to quantify the effects of the geomagnetic phase on winds and vertical total electron content (VTEC) responses over Oukaimeden Observatory. Finally, the last section is devoted to conclusions.

2. Data and Method

2.1. Fabry-Prot Interferometer

The Fabry-Prot interferometer used in this study is located at the Oukaimeden Observatory in Morocco (31.206°N, 7.866°W; 22.84°N magnetic; 2,700 m altitude) and is described in detail in Makela et al. (2009), Kaab et al. (2017), and Malki et al. (2018). To estimate the thermospheric wind speed, the FPI measures the Doppler shift of the 630.0-nm spectral emission emanating from the thermosphere located around an altitude of 250 km. The FPI is composed of a sky scanner system containing two mirrors with double axes that can be rotated to point to any direction (azimuth/zenith), a 42-mm diameter etalon with an air gap spacing of 15 mm, a narrow band interference filter to isolate the emission of interest, and a thermoelectrically cooled CCD to capture the interference pattern produced by the etalon. The resultant interference pattern is analyzed using the methodology described in Harding et al. (2014).

A typical observation mode is a cycle through a series of five specified azimuth and elevation directions (zenith, east, north, west, and south). Individual exposure times for each observation varies depending on the brightness of the emission and typically range from 30 s to 10 min. In addition, regular observations of a frequency-stabilized HeNe laser are made and provide an estimate of the optical transfer function of the instrument. When combined with observations made in the zenith direction, a zero reference required to estimate the absolute Doppler shift is obtained.

For creating climatologies of the thermospheric winds, we adopt the method detailed in Fisher et al. (2015) and Kaab et al. (2017). We sort and bin the filtered data into 15-min intervals and, for each interval, calculate a weighted average, v_m , and sample variability, e , such that

$$v_m = \frac{\sum_i^N v_i \cdot w_i}{\sum_i^N w_i} \quad (1)$$

and

$$e = \sqrt{\frac{1}{N-1} \sum_i^N (v_i - v_m)^2}, \quad (2)$$

where v_i , $w_i = \frac{1}{\sigma_i^2}$, and N are, respectively, the value of the wind (zonal or meridional), its weight (the inverse of its uncertainty, σ_i , squared), and the number of measurements in the given bin. The altitude of the 630.0-nm peak emission is about 250 km (Link & Cogger, 1988). At this altitude, measurements

Table 1

The Classification of Days According to the Two Geomagnetic Indices K_p and $SYM-H$

Classification of days	$SYM-H$	K_p	Number of nights
quiet days	≥ -20	≤ 2	504
Moderate days	$-50 < SYM-H < -20$	$2 < K_p < 5$	245
Disturbed days	≤ -50	≥ 5	41

taken while looking north and south (east and west) are separated by 500 km. We average the north and south (east and west) measurements to obtain the meridional (zonal) wind estimates.

To study the thermospheric climatology above the Oukaimeden Observatory, we present FPI data obtained over 3 years (from 2014 to 2016). A total of 790 nights were classified according to two geomagnetic indices, $SYM-H$ and K_p , as indicated in Table 1. There are 504 quiet nights with $SYM-H \geq -20$ and $K_p \leq 2$, 245 moderate nights with $-50 < SYM-H < -20$ and $2 < K_p < 5$, and 41 disturbed nights $SYM-H \leq -50$ and $K_p \geq 5$. The climatology of each classification (quiet, moderate, and disturbed days) will be presented.

2.2. VTEC From The Global Positioning System

The global positioning system (GPS) has become a useful tool for studying the Earth's atmosphere and, in particular, the ionosphere through measuring the total electron content (TEC), which represents the integrated number of electrons per m^2 along the line of sight from the transmitter on a satellite to the receiver (Boutiouta & Belbachir, 2006; Chauhan & Singh, 2010; Sethi, 2001). In this study, we present the VTEC over Rabat ($33.998^\circ N$, $6.853^\circ W$), obtained from the International GPS Geodynamics Service (IGS) network. The VTEC is determined by integration of the electron density on a perpendicular to the ground standing route; the slant TEC (STEC) is obtained by integrating over any straight path. The procedure for extracting the TEC from GPS data is reported in several documents (Christian et al., 2013; Klobuchar, 1996; Sardon et al., 1994; Schaer et al., 1999; Zoundi et al., 2012).

Parameters (GPS signal and phase, satellite position, the satellite clock biases, etc.) used to calculate the VTEC are extracted from files stored in RINEX (Receiver INdependent EXchange) and IONEX (IONosphere EXchange Format) formats.

2.3. Superposed Epoch Analysis

The $SYM-H$ index has been used to quantify the state of the magnetosphere and the magnitude of storms. From the time evolution of this index, one may identify the initial, main, and recovery phases of a geomagnetic storm (Figure 1). These phases shall be defined as follows: $SYM-H$ equal to -15 nT is taken as the beginning of the initial phase and the end of the recovery phase. The beginning of the main phase was identified as the maximum value of $SYM-H$. The end of the main phase was identified as the minimum value of $SYM-H$ reached.

Storms were superposed in a way similar to Yokoyama and Kamide (1997) and Hutchinson et al. (2011). The average duration of individual storm phases (initial, main, and recovery) was found for different storm size categories and onset mechanisms. The individual storm phases in each were then adjusted to the normalized phase time indices. This was done by shifting the data timestamps to ensure common points in the storm progression. The start time of each phase is essentially a common reference time for the superposition. However, the adjustment of each individual storm phase length to the average duration of the storm phases is vital in ensuring good alignment of the superposition. In practice, for each storm in our data set, we determine the length of its initial phase, and we scaled (increase or decrease) it to the average duration of all the initial phases of the storms. This is done by shifting the data timestamps. Likewise, we adapt the main phase and the recovery phase to their corresponding average duration. Once performed for each time intervals (storms), the data ($SYM-H$ or thermospheric wind speed) corresponding to all time intervals are averaged.

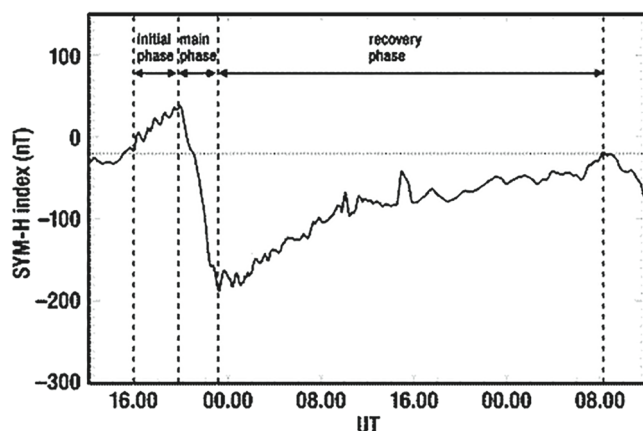


Figure 1. A characteristic $SYM-H$ index storm trace showing initial, main, and recovery phases after Yokoyama and Kamide (1997)

2.4. The Horizontal Wind Model

We have run the horizontal wind model (HWM) (Drob et al., 2015) to compare its results to our data. This model provides an estimate of the meridional and zonal components of the wind for a set of geophysical parameters: latitude, longitude, altitude, and geomagnetic conditions through a 3-hr ap index. HWM model has two components (quiet time HWM14 + disturbance wind model DMW07 Emmert et al., 2008). It is an improved version of the original models HWM87 (Hedin & Spencer, 1988), HWM90 (Hedin, 1991), HWM93 (Hedin et al., 1996), and HWM07 (Drob et al., 2008). With its diverse database of observations, HWM provides a framework for statistical comparison of various measurements in the upper atmosphere. HWM also provides a background of wind fields for wave propagation studies (Drob et al., 2008).

In order to have a more accurate comparison of the FPI data set with the model, we have run the model at each of the four points where the FPI line of sight intersects the altitude 250 km. The geographic coordinates of these four point are as follows: north: 33.406°N, 7.866°W; south: 29.006°N, 7.866°W; east: 31.206°N, 10.066°W; west: 31.206°N, 5.666°W. Then the modeled average meridional and zonal winds have been calculated following the same procedure as with the measured FPI data (see Section 2.1).

3. Results and Discussion

3.1. Thermospheric Wind Variability

Before presenting and commenting on the behavior of thermospheric wind variability over Oukaimeden Observatory during geomagnetic quiet and disturbed conditions, we first begin by presenting the earlier studies relative to ours. Among these studies, there are the climatologies of nighttime upper thermospheric winds measured by ground-based FPIs above several stations during geomagnetically quiet conditions as a function of the local time, latitudinal, seasonal, and cycle dependence was discussed (Emmert et al., 2006a). In parallel, there is a study using the same data set as ours, but analyzed regardless of geomagnetically conditions presented by Kaab et al. (2017). The effect of the 27 February 2014 geomagnetic storm on the thermosphere and the ionosphere is discussed in Malki et al. (2018). The novelty of this paper is the study of the variations of the neutral winds during geomagnetically quiet and disturbed conditions over 3 years of measurements.

Figures 2 and 3 show seasonal variability with the solar cycle of meridional and zonal winds over 3 years 2014, 2015, and 2016 for all data of FPI and HWM model considered in this study. We note that, in general, for the portion of the solar cycle captured by this data set, the winter zonal wind does not show a dependence on solar flux. The eastward component of the zonal winds decreases with the declining solar cycle. This is likely due to enhancement of ion drag due to increasing solar activity; in fact Liu et al. (2009) has found that the fast thermospheric wind jet aligns with the dip equator and not the geographic equator. There is a slight dependence on the reversal time in summer months, with the reversal time from eastward to westward shifting slightly to earlier hours with the declining solar cycle. For autumn and spring months, zonal winds abate before sunrise in 2014 and reverse to the westward direction in 2015 and 2016 months. The time of reversal depends on the solar cycle. We can also observe that the magnitude of the westward component of the zonal wind tends to be smaller at the maximum solar cycle and this variation is in agreement with most previous of midlatitude and low-latitude climatologies (e.g., Biondi et al., 1999; Buonsanto & Witasse, 1999; Emmert et al., 2006a; Fejer et al., 2002). However, Hernandez and Roble (1984) found the opposite at midlatitude site with larger westward zonal winds for solar maximum than solar minimum. We also noticed that the meridional winds during winter time slightly depend on the solar cycle. For the other seasons, the magnitude of the equatorward component of the meridional wind increases with the declining solar cycle. These results of meridional neutral winds are consistent with the change of meridional neutral winds with solar cycle observed at Arecibo and Millstone Hill reported by Emmert et al. (2006a). Hagan (1993) suggest that the solar cycle dependence could be due to changes in the relative importance of high-latitude heating and momentum sources.

The general feature of the measured wind agrees with the model results, particularly for meridional wind. Concerning the zonal winds, some disagreements are observed between the model results, and the data are hypothesized to be due to the fact that the model is not solar cycle sensitive. However, for the remainder of this study, these slight variations as a function of the solar cycle are less pertinent than the larger

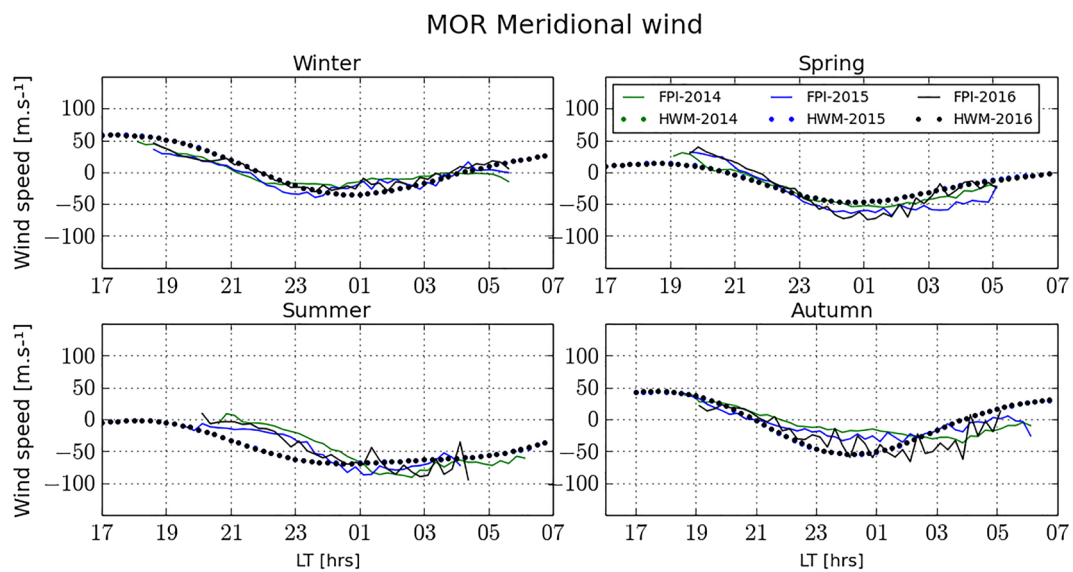


Figure 2. Seasonal variability with the solar cycle of meridional winds over 3 years 2014, 2015, and 2016 of FPI (solid lines) and HWM model (dotted lines).

variations between quiet and disturbed conditions. Thus, we concentrate on interpreting the winds averaged over 3 years.

Figure 4 shows the average zonal and meridional winds as a function of day of the year and local time for quiet days (top set of plots) and disturbed days (bottom set of plots) for 3 years of FPI (left set of plots) and HWM model (right set of plots). The quiet time meridional thermospheric winds show the nighttime wind direction is equatorward (southward) with maximum speed around midnight. The equatorward wind is strongest during the local summer months (June through August). A general abatement of equatorward wind is seen in the local autumn and winter months (September to February), with the meridional winds being poleward (northward) in the early evening with the maximum speed during local autumn and winter

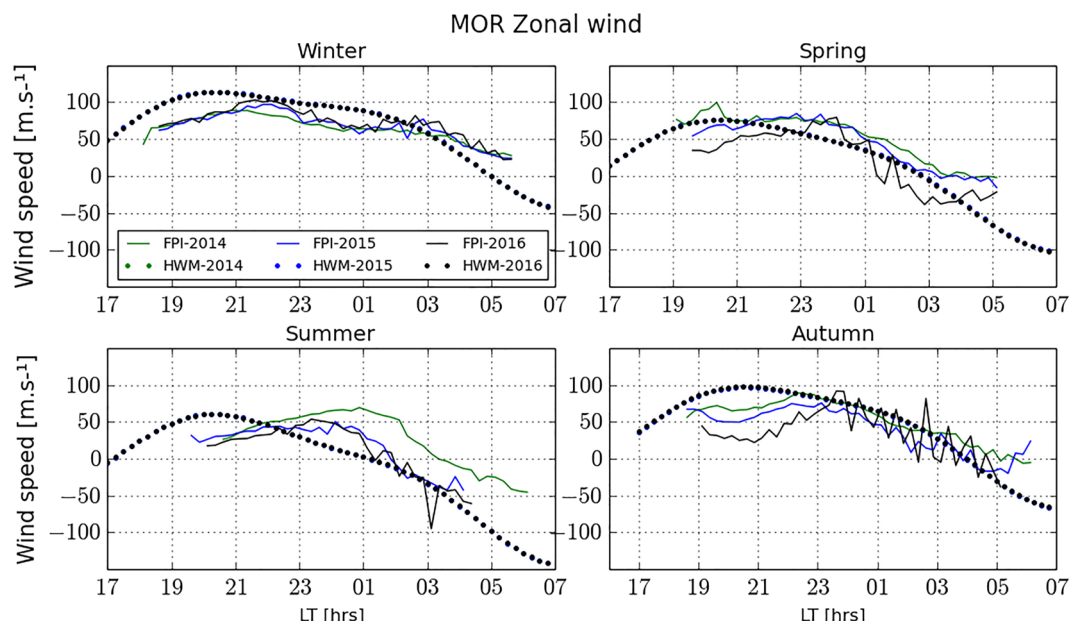


Figure 3. Seasonal variability with the solar cycle of zonal winds over 3 years 2014, 2015, and 2016 of FPI (solid lines) and HWM model (dotted lines).

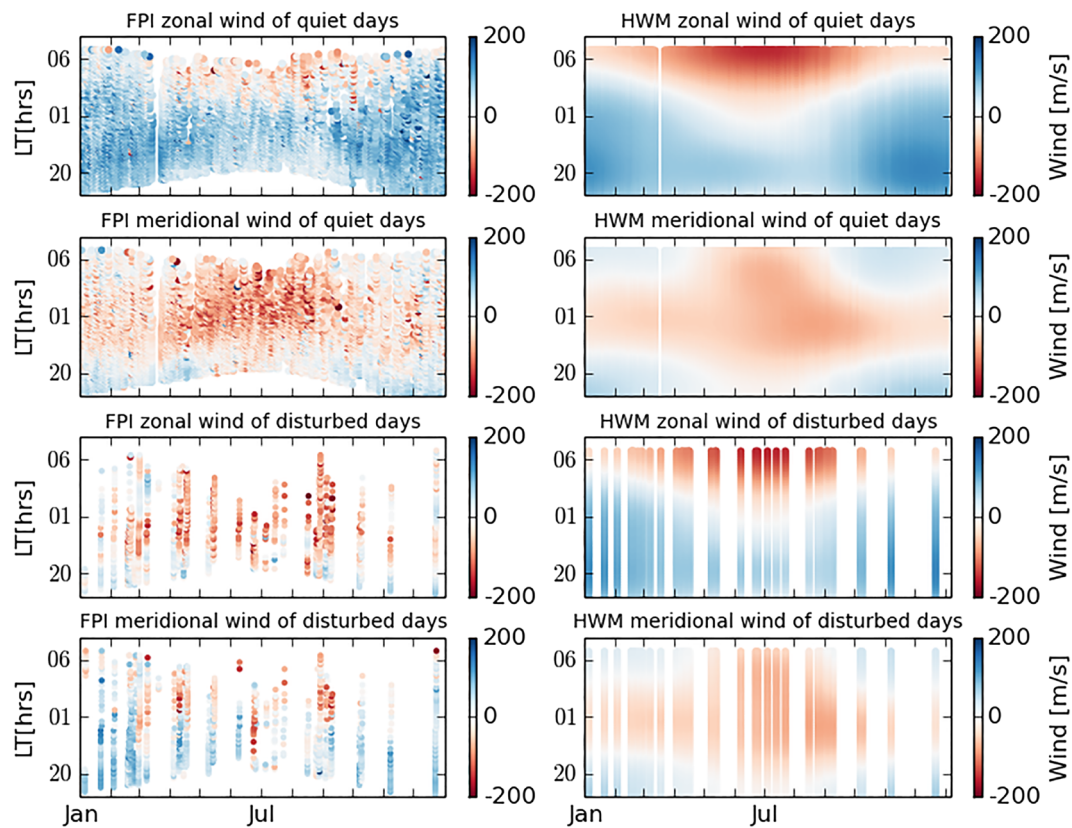


Figure 4. Daily variation of zonal and meridional wind speed as a function of the local time of quiet days (top set of plots) and disturbed days (bottom set of plots) for 3-year average of FPI (left set of plots) and HWM model (right set of plots) and disturbed (bottom panel) are represented. Positive values are eastward for zonal winds and northward for meridional ones.

months (September to February). They reverse to the equatorward direction at 21 LT with a small amplitude speed in the late hours of the night.

The quiet zonal winds show an eastward wind direction on all nights with a postmidnight westward reversal occurring during summer only. An eastward peak occurs during spring (March through May) and summertime around 23 LT and in autumn around 00 LT. Two peaks in the eastward flow occur in wintertime; the first one happens at approximately 22 LT and the second at approximately 02 LT.

Turning attention to the disturbed zonal winds shown in the bottom four panels of Figure 4, we note that in storm time thermospheric winds deviate from their usual quiet time climatology in a variety of ways depending on the season, the magnitude of the storm, the dynamics of the storm energy release, and the time of the storm. When the energy deposition at high latitudes is impulsive (Malki et al., 2018), TADs propagate from high to low latitudes and into the opposite hemisphere. A storm-induced Hadley cell is created flowing in the opposite direction from the quiet time one, with equatorward and westward winds. As this TAD propagates away from the source region, its effects would be measurable by FPIs in both hemispheres. Thus, for a site at northern low latitudes, such as the Oukaimeden Observatory, we would expect to first see a TAD perturbing the background winds in a southward and westward direction (driven by energy input in the northern high latitudes), followed by a perturbation in the northward and westward direction (driven by the energy input in the southern high latitudes). However, depending on the timing of the energy input and the characteristics of the TAD propagation (e.g., propagation velocity), the FPI may not observe both perturbations, due to the instrument's limitation to observe only during nighttime.

As shown in Figure 4, we can see in all seasons the equatorward storm surges and trans-equatorward surges in the meridional winds. The disturbed zonal winds, consisting of the storm winds minus the average quiet time winds, are westward. This result of westward and equatorward winds during the magnetic storm is

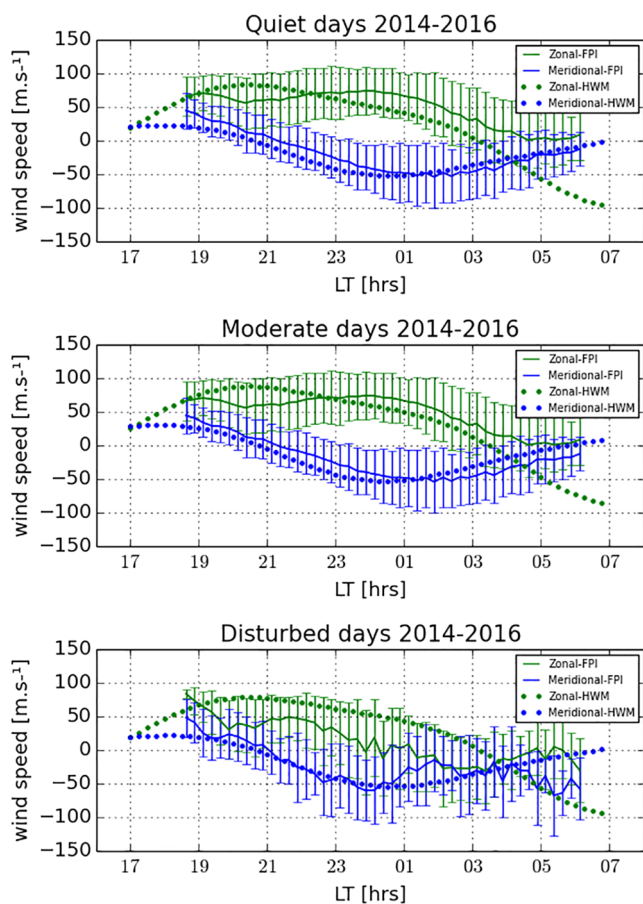


Figure 5. Average speed of meridional (blue) and zonal (green) neutral winds as a function of local time, of 3-year measurements, from 2014 to 2016 of FPI data (solid lines) and HWM model (dotted lines). Quiet nights (top panel), moderate (middle panel), and disturbed (bottom panel) are represented. Positive values are eastward for zonal winds and northward for meridional ones.

consistent with previous results obtained with ground-based FPIs (e.g., Meriwether, 2008). Xiong et al. (2015) also reports that the zonal wind disturbance is mainly westward and increases with magnetic activity and latitude. Furthermore, Emmert et al. (2004) reported westward and equatorward nighttime disturbed winds at midlatitude.

The overall behavior of zonal and meridional winds during quiet time is in good agreement with the model predictions. However, model results give only slight differences between quiet and disturbed nights. The model predictions do not provide accurate direction of the disturbed zonal and meridional winds.

To further investigate the effects of geomagnetic disturbances on the thermospheric neutral winds, we next create annually average winds to serve as a baseline to understand the disturbance effects. Figure 5 shows the average meridional (blue) and zonal neutral winds (green) as a function of local time for quiet, moderate, and disturbed days from 2014 to 2016 (solid lines). The error bars drawn in Figure 5 indicate the range of geophysical variability for each 15-min bin and are calculated as the weighted standard deviation of these data. HWM model (dotted lines) estimates are presented along with the corresponding data (quiet nights: top panel; moderate nights: middle panel; and disturbed nights: bottom panel). Our quiet time results are used primarily as a reference to be compared to more disturbed periods and for extracting the winds perturbation during geomagnetically active periods. From the top panel of Figure 5, the average zonal wind is eastward with a speed of 60 m/s in the early evening hours followed by a slight decrease before a peak amplitude of ~75 m/s is reached around midnight. The zonal wind reduces until the amplitude reaches approximately zero immediately before sunrise. The average meridional neutral wind speed shows poleward speeds of approximately 50 m/s in the early evening hours, reversing to equatorward flow around 21 LT with a maximum speed of 50 m/s from midnight to 03 LT and with weaker winds in the late-night hours.

The middle panel shows the average zonal and meridional neutral wind speed for moderate days over 3 years from 2014 to 2016 above the Oukaimeden observatory, which is very similar to the quiet time winds described above. The annual average of zonal and meridional neutral wind speed moderate days is similar to those of quiet days with slight differences in amplitude, especially after 22 LT. The zonal winds have a maximum speed of 60 m/s at approximately 22:30 LT, then reversing to westward between 03 and 05:30 LT with a small amplitude of 20 m/s and abating before dawn. During the night, the quiet and moderate annual averages of the meridional winds are very similar, although the meridional winds on moderate days is slightly weaker (of approximately 10 m/s).

The bottom panel presents the annual average zonal and meridional neutral wind speed for disturbed days over 3 years from 2014 to 2016. The averaging of data ignores complexities such as the relative time between the beginning of the storm and observations, and so not all features of the effects on the thermospheric wind system are expected to be seen in this treatment (a superposed epoch analysis is presented below, which removes this shortcoming). However, a consistent effect is seen in the zonal winds, which are eastward with an amplitude of 80 m/s at 18:40 LT decreasing to 25 m/s at 20 LT, increasing again to 50 m/s at around 22 LT, and reversing westward around 01 LT. The westward speed is about 40 m/s at 03 LT, decreasing until 05 LT and increasing again. This indicates that there is a general and long-lasting westward perturbation.

In contrast, the meridional winds during disturbed conditions when averaged in this sense do not show much difference from the quiet time average. The average of disturbed meridional winds are northward in the early evening hours and reverse to the equatorward direction at 21 LT and remain in this direction

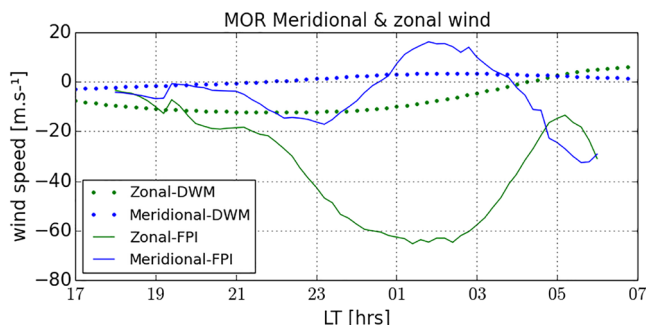


Figure 6. Storm-induced zonal and meridional neutral winds of FPI (solid lines) and HWM model (dotted lines), representing the difference between the disturbed and quiet time data as a function of local time.

ward during the entire night, starting with very low amplitudes as 5 m/s in the early evening hours and increasing to 65 m/s around 02 LT. They then decrease again and reach an amplitude of 15 m/s around 05 LT and increase until dawn. A subsequent change in the zonal circulation flowing westward takes place due to the Coriolis forces (Sean et al., 2007). However, very interesting features appear in the dynamics of the meridional winds. They start equatorward in the early evening hours and reverse to poleward direction around 01 LT. The maximum amplitude of 15 m/s is achieved at 02 LT, followed by an equatorward reversal at 04 LT. The first TAD coming from the Northern Hemisphere reaches the site before the transequatorial one coming from the Southern Hemisphere. This is normal, given the geographical location of the Oukaimeden observatory at 31.206°N. Figure 6 exhibits a clear local-time signature of the annually averaged disturbance winds, given the fact that the time of the storm onset and its duration are randomly distributed. The equatorward wind surges during storm periods at midlatitude stations have been the subject of several studies (e.g., Buonsanto, 1990, 1995; Buonsanto & Witasse, 1999; Buonsanto et al., 1992; Emery et al., 1999; Hernandez et al., 1980; Malki et al., 2018; Yagi & Dyson, 1985). They are observed during storm times and result primarily from pressure gradients generated by high-latitude joule heating and ion drag.

The model predictions give accurate general features of the averaged storm-induced winds. Indeed, the zonal winds predicted are westward during the entire night, where the meridional winds are characterized by the first TAD coming from the north following by the second TAD coming from the south at 23 LT. These features of zonal and meridional winds agree with the observations, but with the significantly general different amplitudes.

3.2. Seasonal Variability

Seasonal behavior of zonal winds for disturbed nights (solid green) and quiet nights (solid blue) as a function of local time is presented in Figure 7. The solid black line is the sliding average of geomagnetically disturbed data. HWM model output is also presented for quiet (blue dots) nights. For disturbed days we have 11 nights in winter, 12 nights in fall, 11 nights in summer, and 7 nights in autumn. For quiet days, we have 125 nights in winter, 158 nights in spring, 145 nights in summer, and 76 nights in autumn. Zonal winds of quiet nights are eastward at the beginning of the night in all seasons and increase for the first several hours after sunset. A maximum eastward speed of 100 m/s in winter and autumn is observed at around 23 LT. This maximum eastward flow transitions to later times and smaller amplitudes during the equinox periods and at local summer with a speed of 75 m/s around midnight. After the maximum eastward flow is reached, a gradual decrease is seen during winter, spring, and autumn; a westward reversal around 03 LT is observed in summer.

The disturbed winds show a general decrease in the eastward flow of the zonal winds related to geomagnetically quiet nights. The maximum difference in amplitude between the quiet and disturbed nights is 50 m/s for winter and spring seasons. In summer and autumn, the maximum difference between quiet and disturbed zonal winds is about 75 and 100 m/s, respectively. The shape of the quiet and disturbed times data might hide information concerning the superpositions of tides and planetary waves (Forbes, 1982). For example, we notice a modulation of wind speed in wintertime both for quiet and disturbed data. Emery

until dawn. They achieve a speed of 60 m/s around midnight, gradually decrease to 40 m/s around 02 LT, and increase to 100 m/s at 05:45 LT and decrease again. To further investigate the effects of geomagnetic disturbances on the thermospheric neutral winds.

It is interesting to note that the estimates from HWM, in an annual sense, characterize the thermospheric winds over this location quite well (except for the slight reduction in zonal winds immediately after sunset).

To isolate the effect of geomagnetic storms on thermospheric winds, we present in Figure 6 the smoothed storm-induced meridional and zonal winds. The storm-induced winds are the difference between the annually averaged disturbed and quiet time data (the top panel minus the bottom panel of Figure 5), for the zonal and meridional components of the winds. The storm-induced zonal winds are west-

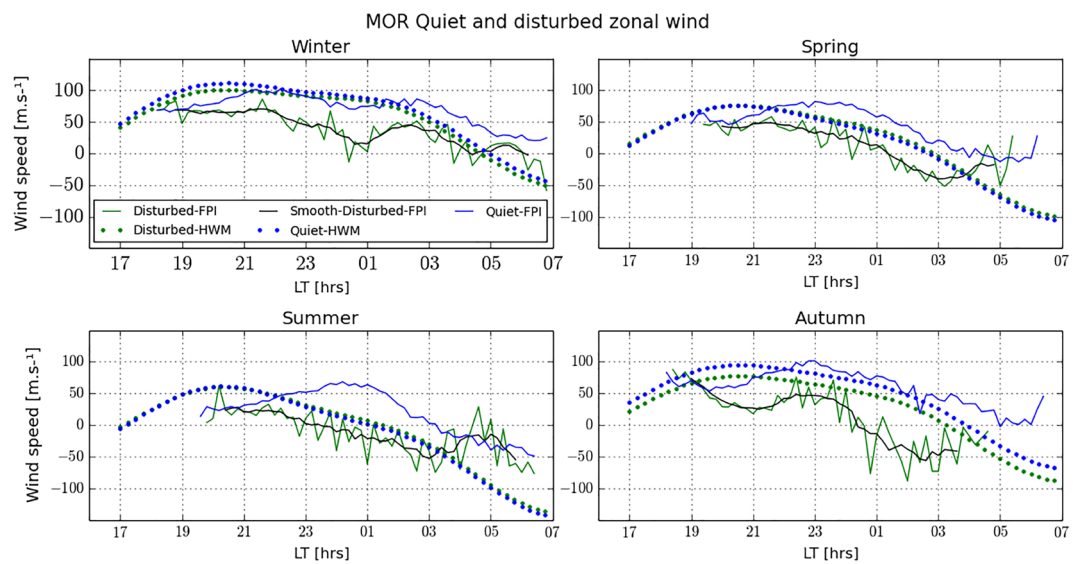


Figure 7. Seasonal behavior of zonal winds for disturbed (green) and quiet nights (blue) as a function of local time, for 3-year measurements from 2014 to 2016 of FPI (solid lines) and HWM (dotted lines). The solid black line is the sliding average of geomagnetically disturbed data. Positive values are eastward.

et al. (1999) reported significant gravity waves in wintertime with phase speeds of approximately 700 m/s ($22^{\circ}/\text{hr}$) observed in the neutral temperature and wind fields during the 2–11 November 1993 storm period. Seasonal behavior of meridional winds for disturbed nights (solid green) and quiet nights (solid blue) as a function of local time is represented in Figure 8 following the same format as Figure 7. Positive values are northward. Meridional winds are poleward in the early evening hours with speeds of approximately 50 m/s in summer and winter and 25 m/s in spring. They reverse to equatorward flow around 21 LT for both quiet and disturbed days. No poleward flow is observed in the summertime. Equatorward flow is observed in the middle of the night with speeds of 80 m/s in summer and spring. We can notice the signature of traveling

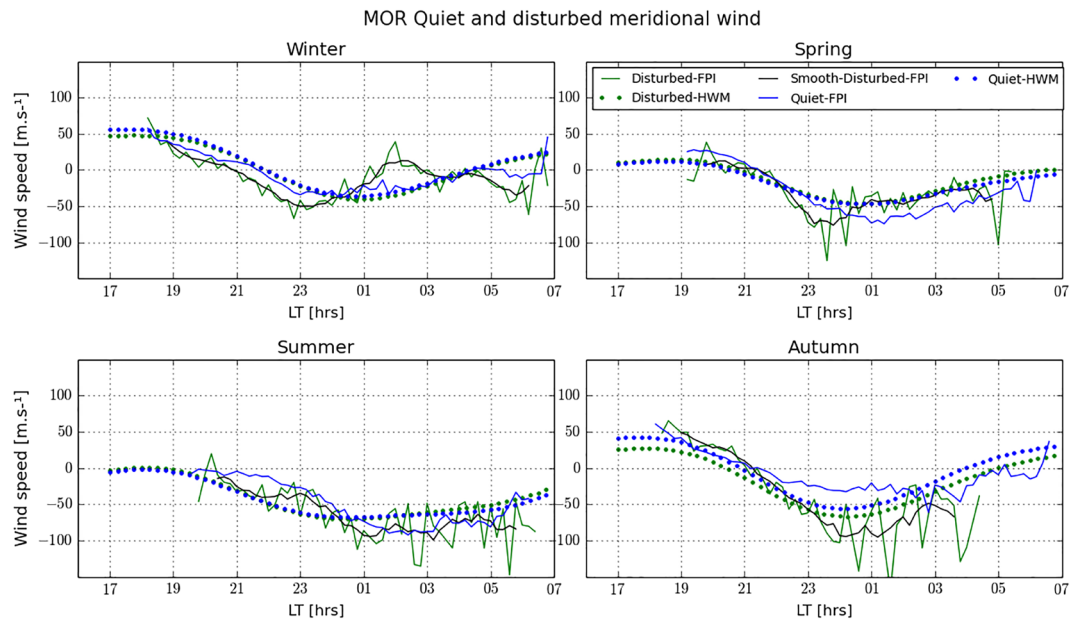


Figure 8. Seasonal behavior of meridional winds for disturbed (green) and quiet nights (blue) as a function of local time, for 3-year measurements from 2014 to 2016 of FPI (solid lines) and HWM (dotted lines). The solid black line is the sliding average of geomagnetically disturbed data. Positive values are northward.

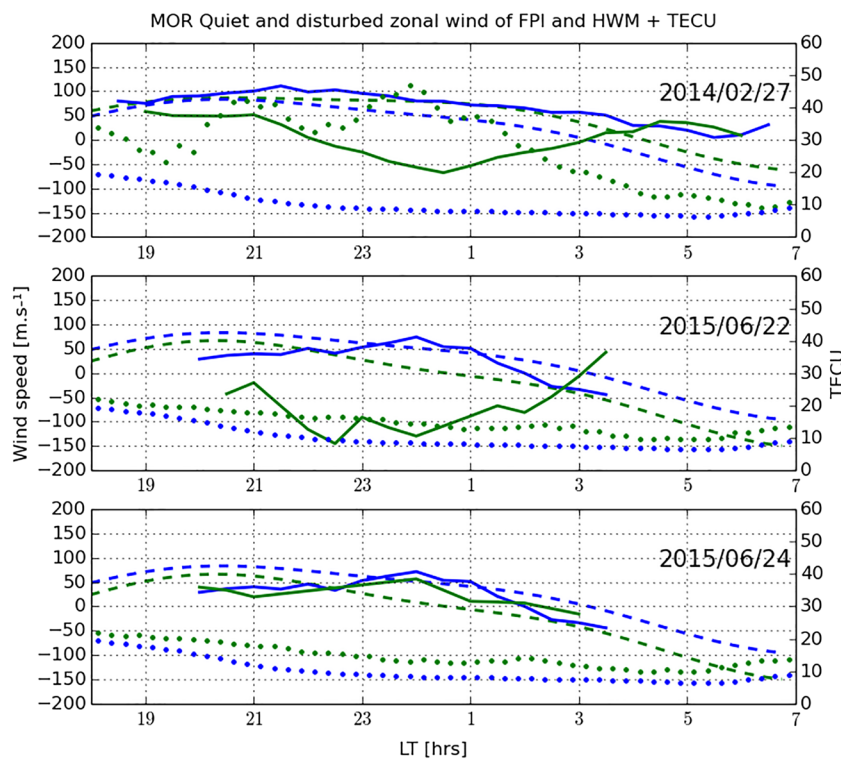


Figure 9. Three examples of the response of the zonal winds to geomagnetic storm. The FPI data (solid lines), HWM model (dashed lines), and vertical total electron content (VTEC) (dotted lines) of disturbed (green) and quiet (blue) are shown. Quiet nighttime data are the median of 30 nights (15 nights before the storm and 15 nights after). Quiet nighttime of TEC data are the average of the quiet nighttime over 2015. The storms selected are the ones with $SYM-H \leq -50$ and $K_p \geq 5$. Positive wind values are eastward.

atmospheric disturbances in the disturbed wind features in winter, spring, and autumn. In the summertime, surprisingly, there are only very slight differences between quiet and disturbed measurements.

Quiet time HWM model predictions illustrate clear seasonal dependence. Slight differences are observed between quiet and disturbed model predictions for both zonal and meridional winds. The model underestimates the westward and equatorward flows injected during the geomagnetic storm.

3.3. Classification of Storm Data

Figure 9 shows three types of responses typical of the data of the zonal winds to geomagnetic storms. Complete analysis of the zonal winds of disturbed nights of each individual geomagnetic storm (41 storms occurring in the 2014–2016 period as indicated in Table B1 have been carried out). We have classified the zonal neutral wind during the geomagnetic storm to two types of variation. We have eliminated from the statistics the nights that are not well covered with data (14 nights among 41 geomagnetic storms). The first type is a westward perturbation from the typical eastward flow. In 70% of the 27 remaining cases, the flow reverses to the westward direction. The zonal thermosphere wind is stronger before midnight in 16% of the cases (see an example of these cases in the middle panel of Figure 9) and after midnight in 54% of the cases (see an example of this type in the top panel of Figure 9), with a magnitude varying from 20 to 175 m/s. The second type seen in the database, accounting for the other 30% of cases, only a slight perturbation in the zonal wind is observed (see an example of this type in the bottom panel of Figure 9). In general, perturbation of the zonal winds in early evening hours and before dawn is quiet small in 74% of cases. For the VTEC, we can notice that in the first type with the peak before midnight, there is an increase in VTEC over the whole night. However, for the second type, there is only a slight variation of the VTEC between the quiet and disturbed days.

Figure 10 shows a similar presentation for the meridional winds. The disturbed meridional wind is characterized mainly by two types of variations. The first type is characterized by TAD-induced circulation: an

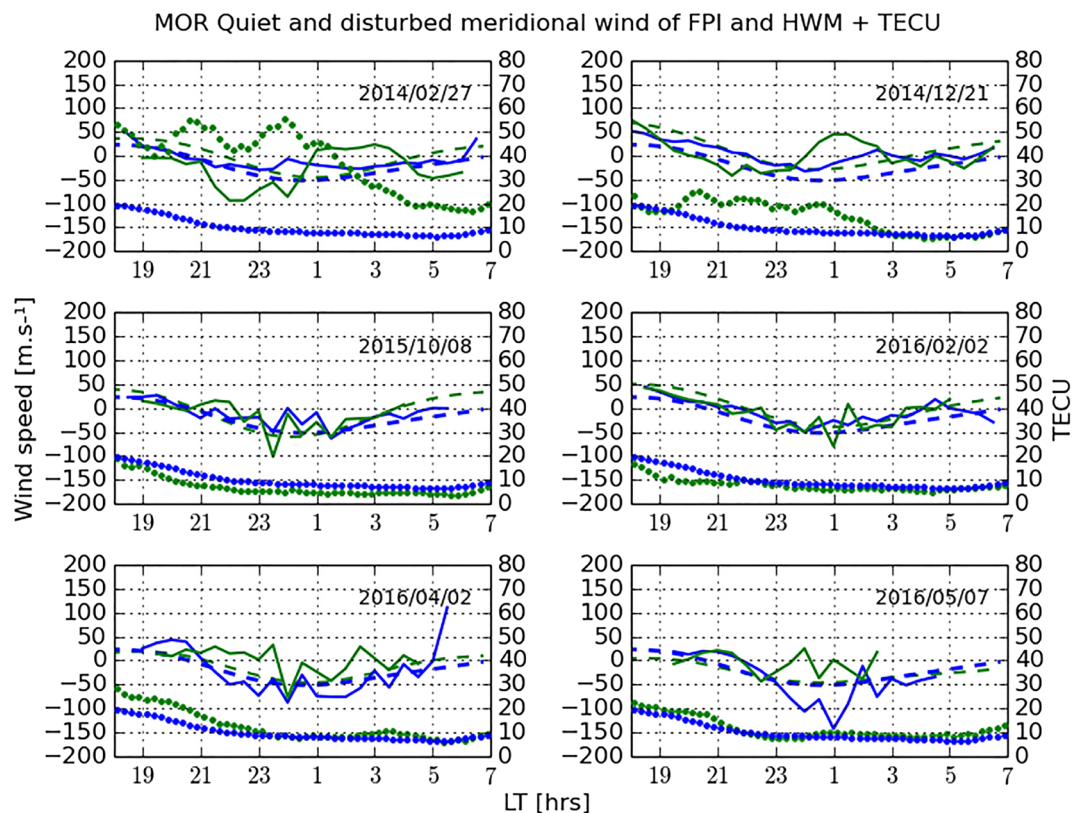


Figure 10. Six examples of the response of the meridional winds to geomagnetic storms. The FPI data (solid lines), HWM model (dashed lines), and vertical total electron content (VTEC) (dotted lines) of disturbed (green) and quiet (blue) are shown. Quiet nighttime data are the median of 30 nights (15 nights before the storm and 15 nights after). Quiet nighttime of TEC data are the average of the quiet nighttime over 2015. The storms selected are the ones with $SYM-H \leq -50$ and $K_p \geq 5$. Positive values are northward.

equatorward perturbation, indicative of the first TAD coming from the north followed by a poleward perturbation, indicative of the second TAD, coming from the south. The timing of the first TAD and the duration of each TAD can be different in each case. For example, Malki et al. (2018) reported that the meridional winds reacted to the transequatorial southern TAD at 00:20. Its effect lasted for 3.5 hr during which the southern measurement location had a larger speed than the northern one. Examples of disturbed nights of this type are 27 February 2014, 21 December 2014, 15 April 2015, 16 April 2015, 13 May 2015, 7 June 2015, 22 June 2015, 15 August 2015, 27 August 2015, 20 January 2016, and 6 November 2015. The storms of this type account for 59% of cases. The example of this first type is illustrated in the two top panels of Figure 10. We observe a good anticorrelation between the VTEC and the meridional wind: southward winds correspond to high VTEC values before midnight. However, we observe a decrease of the TEC and an absence of correlation with the meridional winds during the rest of the night. The observed anticorrelation is probably caused by the TAD. At night, plasma production is almost close to zero, but in this first type of disturbed night, there is an increase in the TEC. This can only be due to transport. This observation is consistent with previous studies discussing the negative correlation between $hmF2$ and $NmF2$ during the passage of a TAD, at least in the initial phase (Bauske & Prolss, 1997; Lee et al., 2002, 2004).

The second type is characterized by only slight perturbation in both VTEC and neutral winds. Examples of disturbed nights of the second type are 27 August 2014, 12 May 2015, 13 July 2015, 22 July 2015, 26 August 2014, 7 September 2014, 8 September 2015, 8 October 2015, 2 February 2016, and 7 April 2016 and account for 33% of the cases. Two examples of this second type are presented in the middle panels of Figure 10. We notice that on some nights, we can observe more than two TADs in the first type. However, we have observed in two nights (2 April 2016 and 7 May 2016) the transequatorial wind whole the night with the slight

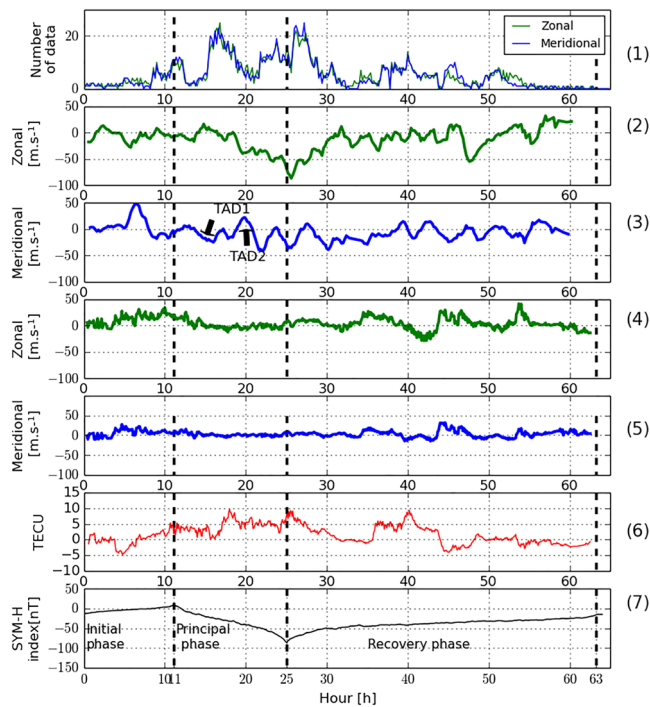


Figure 11. From top to bottom: (1) number of data in each bin of zonal (green) and meridional (blue) neutral wind, (2) superposed of zonal, and (3) meridional neutral wind speed of FPI measurements, (4) superposed of zonal and (5) meridional neutral wind speed of HWM model, (6) vertical total electron content (VTEC) of 43 nights (28 disturbed nights + 15 nights available before or after the disturbed nights) minus their correspondent quite time, and (7) Superposed SYM-H index of the same 43 nights as a function of the time. Quiet nighttime data are the median of 30 quiet nights (15 nights before the storm and 15 nights after). The storms selected are the isolated ones, having SYM-H with clear phases.

and zonal winds is defined as being the measured wind minus the quiet wind. In Figure 11, the sliding average (2-hr window) of this disturbed flow of meridional and zonal winds data is shown.

From the bottom panel of Figure 11, we notice that the average duration of the initial phase for all the magnetic storms is 11 hr, that of the main phase is approximately 14 hr, and that of the recovery phase is approximately 38 hr. From epoch analysis of both meridional and zonal winds, we notice that between the sudden storm commencement (SSC), $t=0$ hr, and the beginning of the main phase, $t=11$ hr, (initial phase), the signature of the second transequatorial (northward) TAD is present with the maximum speed 50 m/s after 6 hr of the beginning of the storm. This variation of the meridional flow is accompanied by the decrease of the VTEC, while the zonal wind is westward with a maximum speed of 25 m/s. At 30 min after the zonal wind reached its maximum, the meridional winds reach its first maximum.

The main phase is characterized predominantly by the occurrence of the first TAD approximately 3 hr after the storm main phase onset with the maximum disturbed meridional wind speed of 25 m/s. Throughout the main phase, the zonal winds become increasingly westward, eventually reaching -80 m/s at the peak of the disturbance, and the VTEC increases. Oliveira et al. (2017) performed a superposed epoch analysis of thermospheric density in response to geomagnetic storms, that choice the density maximizes 12 hr after the beginning of the main phase. This increase in the amplitude of westward winds with magnetic activity is also reported by Fejer et al. (2002). Nadia et al. (2019) reported the same behavior of the increase in VTEC during the storm period, and they are found in the African region; the largest increase in the VTEC is observed for the equatorial latitude station NKLG in Africa (geographic coordinates: 0.35°N , 9.67°E) during the storm. On day after the beginning of storm main phase onset, a negative effect is observed in the northern midlatitude station, whereas for earlier results on low and equatorial storms, Walker (1973) reported for Hong

perturbation of the VTEC. Those two nights are presented in the bottom panels of Figure 10. Given the geographic position of the observatory, this behavior of the second type is unexpected during a geomagnetic storm; one expects the first TAD to come from the Northern Hemisphere. All those cases make us ask the following question: What are the most important parameters that shape the thermospheric response to the geomagnetic storm? Is the declining solar cycle one of them? There may be a relationship between the energy deposition of the geomagnetic storm and the ignition on some wave modes that shape the TAD-like behavior. Or it is explained by either the propagation velocities of the two TADs are different or by the asymmetries in the amount of joule heating produced during a storm and the onset times.

3.4. Superposed Epoch Analysis

To determine the temporal response of the low-latitude thermosphere to magnetic storms and the effect of each phase of magnetic storms (initial, main, and recovery) on thermospheric winds, the superposed epoch analysis method was applied to 28 disturbed events. They are isolated geomagnetic storms, in which there is only one storm and it is easy to determine each phase plus 15 nights available in the initial and recovery phases. Those 15 nights are selected to complete the profile of all hours of the storm evolution.

Figure 11 shows from top to bottom: number of data in each bin of zonal (green) and meridional (blue) neutral wind, average of zonal, meridional of neutral wind speed, and VTEC of 43 nights (28 disturbed nights + 15 nights available before or after the disturbed night; see Table B1) minus their correspondent quite time and superposed SYM-H index of the same 43 nights as a function of time. Quiet nighttime data are the median of 30 nights (15 nights before the storm and 15 nights after). The storms selected are the isolated ones, having SYM-H with clear phases. The disturbed flow of meridional

Kong (geomagnetic latitude 10.9) that SSC occurring during the daytime was sometimes preceded by a slight increase but often followed by a sharp decrease in VTEC, and that is precisely what we observed in the recovery phase. Van de Heyde (2012) reported the relationship between geomagnetic and ionospheric storms; they notice that large changes in the ionosphere occur even in the prestorm period and can be at least as large as those observed during storms, sometimes even more. As for meridional winds in the main phase of the storms, they are characterized by many TADs beginning by a first TAD coming from the north. We can also notice the occurrence of the second TAD (coming from the south) just after the end of the main phase.

The recovery phase is mainly characterized by only minor storm flow. In spring and summer times, we can notice eastward and equatorward storm flows approximately 18 hr after the beginning of the recovery storm phase. We should emphasize that in spring and summer the quiet zonal flow is westward before dawn (see Figure 6). From the thermospheric response during the geomagnetic storm, it can be noted that when the storm is weak, the meridional and zonal disturbed flows are negative or close to zero depending on the intensity of the storm or SYM-H. This negative component indicates that the flow is mainly directed by equatorward and westward (Figures 6 and 7). When the storm is intense, what is observed during the night depends on the time of the occurrence of the storm. For example, when the storm started before sunset, as in the case of the storm 27 February 2014, three TADs are observed (Malki et al., 2018). On the contrary, the storm of 18 February 2014 has the same magnitude but exhibits no TADs or maybe only one observed in late hours. According to our classification of the storms, 41% of them experience two TADs. Inside the first one, coming from the Northern Hemisphere, the disturbed flow is equatorial and westward, which means negative components for both meridional and zonal storm flow. The second TAD occurring later is transequatorial, and its disturbed flow is northward and remains westward with a weaker amplitude.

4. Conclusion

Thermospheric winds are one of the keys to a better understanding of not only the thermosphere but also the ionosphere, due to the coupling between the neutral and ionized fluids. In this paper, we have presented the properties of the thermospheric wind observed over the Oukaimeden Observatory for 3 years. Both the quiet time and disturbed winds have been presented and represent the first extended period of ground-based FPI measurements of midlatitude thermospheric dynamics in North Africa.

From our analysis, we find a slight dependence of the wind on solar flux, evident during the minimum activity seen in 2016. Specifically, a general decrease in the eastward flow of the zonal winds has been observed. We have also observed an increase in the equatorward flow of meridional winds with the declining solar cycle.

Analysis of the data collected under geomagnetically disturbed conditions indicates that storm-induced zonal winds exhibit westward perturbations from the typical wind conditions, while storm-induced meridional winds are characterized by the passage of two to three TADs. In 58% of cases, the zonal winds reverse to the westward direction. In 74% of cases, they are characterized by the slight discrepancies between the disturbed and quiet nights zonal winds in early evening hours and before dawn. We have noticed that what we call the peak of the storm occurs between 18 and 22 LT in 30% of the cases, between 22 and 02 LT in 25% of the cases, and finally between 02 and 06 LT in 45% of the cases. A peak in the westward flow of disturbed zonal winds is observed in 70% of the cases, with a magnitude varying from 20 to 175 m/s.

The disturbed meridional wind is characterized by two types of variation. The first type is characterized by TAD-induced circulation; the first TAD1 comes from the north, and the second TAD2 is transequatorial, coming from the south. These storms with TAD-induced circulation account for 59% of the cases. The second type is when there is a slight discrepancy or the same shape between the disturbed and quiet nights. These cases account then for 33% of the cases.

We have noticed that on some nights we can observe more than two TADs in the first type. However, we have observed in the two nights the transequatorial winds whole the night. Given the geographic position of the observatory, this behavior of the second type is unexpected during a geomagnetic storm; one expects the first TAD to come from the Northern Hemisphere.

Superposed epoch analysis was applied with FPI data to obtain the characteristic temporal variation based on a large number of these transient events. Separate analyses were performed for events of disturbed conditions ($K_p \geq 5$); the “superposed epoch analysis” method was applied to 28 disturbed events. They are isolated geomagnetic storms, in which there is only one storm and it is easy to determine each phase. The main phase is characterized predominately by the occurrence of the first TAD (coming from the north), which has equatorward and westward disturbed flows. We have also noticed that the maximum disturbed flow of zonal winds has occurred at the same time when the SYM-H index reached the minimum. The occurrence of the second TAD is just after the end of the main phase. The recovery phase is mainly characterized by gentle storm flow. Eastward and equatorward storm flows observed in the later hours of the evolution of storm occur mainly in spring and summer times.

Appendix A: List of 41 Disturbed Nights

This table below provides a list of the 41 storms over 3 years from 2014 to 2016.

Table A1
List of 41 Disturbed Nights

Days	Date (YY/MM/DD)—start time	Date (YY/MM/DD)—end time	SMY-H [min] [nT]	Kp [max]
1	2014/02/18—21:30	2014/02/19—6:26	-127.0	6.0
2	2014/02/19—18:56	2014/02/20—4:7	-102.0	6.0
3	2014/02/27—19:3	2014/02/28—6:19	-101.0	5.0
4	2014/04/11—20:37	2014/04/12—5:23	-92.0	5.0
5	2014/08/27—20:37	2014/08/28—6:22	-90.0	5.0
6	2014/12/21—18:15	2014/12/22—6:46	-65.0	5.0
7	2015/01/04—18:22	2015/01/05—6:48	-75.0	5.0
8	2015/02/17—19:0	2015/02/18—6:23	-70.0	5.0
9	2015/02/23—19:3	2015/02/24—6:29	-76.0	5.0
10	2015/03/18—3:18	2015/03/19—4:22	-76.0	5.0
11	2015/04/09—20:42	2015/04/10—2:23	-71.0	5.0
12	2015/04/15—20:37	2015/04/16—5:26	-83.0	5.0
13	2015/04/16—20:41	2015/04/17—5:26	-88.0	6.0
14	2015/05/12—21:3	2015/05/13—3:30	-98.0	6.0
15	2015/05/13—21:6	2015/05/14—4:26	-69.0	5.0
16	2015/06/07—21:19	2015/06/08—5:41	-105.0	6.0
17	2015/06/22—20:26	2015/06/23—3:51	-208.0	8.0
18	2015/06/24—20:22	2015/06/25—3:3	-67.0	5.0
19	2015/07/04—20:22	2015/07/05—2:8	-87.0	5.0
20	2015/07/13—20:19	2015/07/14—3:55	-61.0	6.0
21	2015/07/22—21:33	2015/07/23—5:8	-83.0	5.0
22	2015/08/15—19:56	2015/08/16—2:51	-94.0	6.0
23	2015/08/26—19:44	2015/08/27—5:22	-97.0	6.0
24	2015/08/27—19:41	2015/08/28—5:25	-101.0	6.0
25	2015/09/07—19:27	2015/09/08—2:49	-91.0	6.0
26	2015/09/08—20:4	2015/09/09—3:49	-113.0	6.0
27	2015/10/06—18:49	2015/10/07—2:10	-84.0	6.0
28	2015/10/08—19:18	2015/10/09—4:36	-58.0	5.0
29	2015/11/06—18:18	2015/11/07—3:45	-106.0	6.0
30	2016/01/20—18:36	2016/01/21—6:51	-95.0	6.0
31	2016/02/02—18:47	2016/02/03—5:45	-60.0	5.0
32	2016/02/16—18:59	2016/02/17—6:22	-58.0	5.0
33	2016/02/17—19:0	2016/02/18—6:16	-60.0	6.0
34	2016/03/06—19:12	2016/03/07—6:15	-110.0	6.0
35	2016/04/02—19:32	2016/04/03—4:41	-66.0	5.0
36	2016/04/07—20:7	2016/04/08—5:18	-67.0	6.0
37	2016/04/12—19:38	2016/04/13—5:4	-70.0	5.0
38	2016/05/07—19:59	2016/05/08—2:46	-105.0	6.0
39	2016/08/23—19:47	2016/08/24—5:8	-83.0	5.0
40	2016/09/01—19:34	2016/09/02—4:36	-74.0	6.0
41	2016/09/02—19:45	2016/09/03—4:25	-54.0	6.0

Appendix B: List of 43 Nights Used to Figure 11

This table below provides a list of the 28 storms over 3 years from 2014 to 2016 that used to plot Figure 11.

Table B1

List of 43 Nights Used to Constructed Figure 11

Days	Date (YY/MM/DD)—Start time	Date (YY/MM/DD)—End time	SMY-H [min] [nT]	Kp [max]
1	2014/02/18—21:30	2014/02/19—6:26	-127.0	6.0
2	2014/02/27—19:3	2014/02/28—6:19	-101.0	5.0
3	2014/02/28—19:3	2014/02/29—6:21	-51.0	2.0
4	2014/04/11—20:37	2014/04/12—5:23	-92.0	5.0
5	2014/08/27—20:37	2014/08/28—6:22	-90.0	5.0
6	2014/12/19—18:14	2014/12/20—6:38	-15.0	3.0
7	2014/12/20—18:15	2014/12/21—6:45	-27.0	3.0
8	2014/12/21—18:15	2014/12/22—6:46	-65.0	5.0
9	2015/01/03—18:18	2015/01/04—6:48	-37.0	2.0
10	2015/01/04—18:22	2015/01/05—6:48	-75.0	5.0
11	2015/01/05—18:25	2015/01/06—6:45	-46.0	3.0
12	2015/02/17—19:0	2015/02/18—6:23	-70.0	5.0
13	2015/02/23—19:3	2015/02/24—6:29	-76.0	5.0
14	2015/04/09—20:42	2015/04/10—2:23	-71.0	5.0
15	2015/04/15—20:37	2015/04/16—5:26	-83.0	5.0
16	2015/04/16—20:41	2015/04/17—5:26	-88.0	6.0
17	2015/06/07—21:19	2015/06/08—5:41	-105.0	6.0
18	2015/06/08—22:4	2015/06/09—5:41	-60.0	4.0
19	2015/06/09—21:22	2015/06/10—2:43	-46.0	3.0
20	2015/06/10—21:18	2015/06/11—3:29	-37.0	3.0
21	2015/07/04—20:22	2015/07/05—2:8	-87.0	5.0
22	2015/07/13—20:19	2015/07/14—3:55	-61.0	6.0
23	2015/07/22—21:33	2015/07/23—5:8	-83.0	5.0
24	2015/08/15—19:56	2015/08/16—2:51	-94.0	6.0
25	2015/08/26—19:44	2015/08/27—5:22	-97.0	6.0
26	2015/08/27—19:41	2015/08/28—5:25	-101.0	6.0
27	2015/10/06—18:49	2015/10/07—2:10	-84.0	6.0
28	2015/10/08—19:18	2015/10/09—4:36	-58.0	5.0
29	2015/11/06—18:18	2015/11/07—3:45	-106.0	6.0
30	2016/01/19—18:36	2016/01/20—6:45	-40.0	3.0
31	2016/01/20—18:36	2016/01/21—6:51	-95.0	6.0
32	2016/01/21—18:37	2016/01/22—6:48	-49.0	5.0
33	2016/02/02—18:47	2016/02/03—5:45	-60.0	5.0
34	2016/03/05—19:11	2016/03/06—6:13	-2.0	2.0
35	2016/03/06—19:12	2016/03/07—6:15	-110.0	6.0
36	2016/03/07—19:18	2016/03/08—5:53	-55.0	5.0
37	2016/04/02—19:32	2016/04/03—4:41	-66.0	5.0
38	2016/04/07—20:7	2016/04/08—5:18	-67.0	6.0
39	2016/04/08—19:36	2016/04/09—4:49	-26.0	1.0
40	2016/04/12—19:38	2016/04/13—5:4	-70.0	5.0
41	2016/08/22—19:48	2016/08/23—3:48	-12.0	2.0
42	2016/08/23—19:47	2016/08/24—5:8	-83.0	5.0
43	2016/08/24—19:45	2016/08/25—0:37	-40.0	4.0

Data Availability Statement

The LOS wind data used in this study are freely available for use in the Madrigal database (<http://madrigal.haystack.mit.edu/madrigal/>). The SYM-H index storm can be downloaded online (<https://omniweb.gsfc.nasa.gov/>). The International Service of Geomagnetic Indices (ISGI) is in charge of the elaboration and dissemination of geomagnetic indices (Kp) (from <http://isgi.unistra.fr/>). The GPS data used in this study are freely available for use from the International GPS Geodynamics Service (IGS, 2018) (<ftp://data-out.unavco.org/pub/rinex/obs/>, last access: 6 July 2018) network.

Acknowledgments

This project is financially supported by Campus France through the French-Moroccan bilateral program "PHC Toubkal 2019" (Grant 41409WJ). Work at the University of Illinois at Urbana-Champaign was supported by National Science Foundation CEDAR Grant AGS 16-51298. Please contact Jonathan J. Makela (jmakela@illinois.edu) before using these data.

References

Aruliah, A. L., Farmer, A. D., & Rees, B. A. A. U. (1996). The seasonal behavior of high-latitude thermospheric winds and ion velocities observed over one solar cycle. *Journal of Geophysical Research*, 101(A7), 15,701–15,711. <https://doi.org/10.1029/96JA00360>

Bauske, R., & Prolss, G. W. (1997). Modeling the ionospheric response to traveling atmospheric disturbances. *Journal of Geophysical Research*, 102(A7), 14,555–14,562. <https://doi.org/10.1029/97JA00941>

Biondi, M. A., Meriwether, J. W., Fejer, B. G., Gonzalez, S. A., & Hallenbeck, D. C. (1991). Equatorial thermospheric wind changes during the solar cycle: Measurements at Arequipa, Peru, from 1983 to 1990. *Journal of Geophysical Research*, 96(A9), 15,917–15,930. <https://doi.org/10.1029/91JA01645>

Biondi, M. A., Sazykin, S. Y., Fejer, B. G., Meriwether, J. W., & Fesen, C. G. (1999). Equatorial and low latitude thermospheric winds: Measured quiet time variations with season and solar flux from 1980 to 1990. *Journal of Geophysical Research*, 104(A8), 17,091–17,106. <https://doi.org/10.1029/1999JA900174>

Boutiouta, S., & Belbachir, A. H. (2006). Magnetic storms effects on the ionosphere TEC through GPS data. *Information Technology Journal*, 5, 908–915. <https://doi.org/10.3923/itj.2006.908.915>

Buonsanto, M. J. (1990). *Journal of Atmospheric and Terrestrial Physics*, 52(3), 223–240. [https://doi.org/10.1016/0021-9169\(90\)90126-8](https://doi.org/10.1016/0021-9169(90)90126-8)

Buonsanto, M. J. (1995). Millstone hill incoherent scatter F region observations during the disturbances of June 1991. *Journal of Geophysical Research*, 100, 5743–5755. <https://doi.org/10.1029/94JA03316>

Buonsanto, M. J., Foster, J. C., & Sippler, D. P. (1992). Observations from Millstone Hill during the geomagnetic disturbance of march and april 1990. *Journal of Geophysical Research*, 97, 1225–1234. <https://doi.org/10.1029/91JA02428>

Buonsanto, M. J., & Witasse, O. G. (1999). An updated climatology of thermospheric neutral winds and F region ion drifts above Millstone Hill. *Journal of Geophysical Research*, 104(A11), 24,675–24,687. <https://doi.org/10.1029/1999JA900345>

Burns, A. G., Killeen, T. L., Wang, W., & Roble, R. G. (2004). The solar-cycle-dependent response of the thermosphere to geomagnetic storms. *Journal of Atmospheric and Solar-Terrestrial Physics*, 66(1), 1–14. <https://doi.org/10.1016/j.jastp.2003.09.015>

Chauhan, V., & Singh, O. (2010). A morphological study of GPS-TEC data at Agra and their comparison with the IRI model. *Advances in Space Research*, 46, 280–290. <https://doi.org/10.1016/j.asr.2010.03.018>

Christian, F., Emmanuel, F., & Francois, Z. (2013). CODG TEC variation during solar maximum and minimum over Niamey. *European Scientific Journal*, 9, 74–80. <https://doi.org/10.19044/esj.2013.v9n27p%25p>

Drob, D. P., Emmert, J. T., Crowley, G., Picone, J. M., Shepherd, G. G., Skinner, W., et al. (2008). An empirical model of the Earth's horizontal wind fields: HWM07. *Journal of Geophysical Research*, 113, A12304. <https://doi.org/10.1029/2008JA013668>

Drob, D. P., Emmert, J. T., Meriwether, J. W., Makela, J. J., Doornbos, E., Conde, M., et al. (2015). An update to the horizontal wind model HWM: The quiet time thermosphere. *Earth and Space Science*, 2, 301–319. <https://doi.org/10.1002/2014EA000089>

Duboin, M.-L., & Lafeuille, M. (1992). Thermospheric dynamics above Saint-Saintin: Statistical study of the data set. *Journal of Geophysical Research*, 97(A6), 8661. <https://doi.org/10.1029/92JA00281>

Emery, B., Lathuillere, C., Richards, P., Roble, R., Buonsanto, M., & Knipp, R. (1999). Time dependent thermospheric neutral response to the 2–11 November 1993 storm period. *Journal of Atmospheric and Solar-Terrestrial Physics*, 61(3-4), 329–350. [https://doi.org/10.1016/s1364-6826\(98\)00137-0](https://doi.org/10.1016/s1364-6826(98)00137-0)

Emmert, J. T., Fejer, B. G., Shepherd, G. G., & Solheim, B. H. (2004). Average nighttime F region disturbance neutral winds measured by UARS WINDII: Initial results. *Geophysical Research Letters*, 31, L22807. <https://doi.org/10.1029/2004GL021611>

Emmert, J. T., Fejer, B. G., & Sippler, D. P. (2003). Climatology and latitudinal gradients of quiet time thermospheric neutral winds over Millstone Hill from Fabry-Perot interferometer measurements. *Journal of Geophysical Research*, 108(A5), 1196. <https://doi.org/10.1029/2002JA009765>

Emmert, J. T., Meier, R. R., Picone, J. M., Lean, J. L., & Christensen, A. B. (2006a). Thermospheric density 2002–2004: TIMED/GUVI dayside limb observations and satellite drag. *Journal of Geophysical Research*, 111, A10S16. <https://doi.org/10.1029/2005JA011495>

Emmert, J. T., Picone, J. M., & Meier, R. R. (2008). Thermospheric global average density trends, 1967–2007, derived from orbits of 5000 near-Earth objects. *Geophysical Research Letters*, 35, L05101. <https://doi.org/10.1029/2007GL032809>

Fejer, B. G., Blanc, M., & Richmond, A. D. (2016). Post-storm middle and low-latitude ionospheric electric fields effects. *Space Science Reviews*, 206, 407–429. <https://doi.org/10.1007/s11214-016-0320-x>

Fejer, B. G., Emmert, J. T., & Sippler, D. P. (2002). Climatology and storm time dependence of nighttime thermospheric neutral winds over Millstone Hill. *Journal of Geophysical Research*, 107(A5), SIA 3–1-SIA 3-9. <https://doi.org/10.1029/2001JA000300>

Fesen, C. G., R. R., & Duboin, M.-L. (1995). Simulations of seasonal and geomagnetic activity effects at Saint-Saintin. *Journal of Geophysical Research*, 100(A11), 21,397–21,408. <https://doi.org/10.1029/95JA01211>

Fisher, D. J., Makela, J. J., Meriwether, J. W., Buriti, R. A., Benkhaldoun, Z., Kaab, M., & Lagheryeb, A. (2015). Climatologies of nighttime thermospheric winds and temperatures from Fabry-Perot interferometer measurements: From solar minimum to solar maximum. *Journal of Geophysical Research: Space Physics*, 120, 6679–6693. <https://doi.org/10.1002/2015JA021170>

Forbes, J. M. (1982). Atmospheric tides: 2. The solar and lunar semidiurnal components. *Journal of Geophysical Research*, 87(A7), 5241–5252. <https://doi.org/10.1029/JA087iA07p05241>

Fuller-Rowell, T. J., & Rees, D. (1980). A three-dimensional time-dependent global model of the thermosphere. *Journal of the Atmospheric Sciences*, 37(11), 2545–2567. [https://doi.org/10.1175/1520-0469\(1980\)037<2545:atddtg>2.0.co;2](https://doi.org/10.1175/1520-0469(1980)037<2545:atddtg>2.0.co;2)

Hagan, M. E. (1993). Quiet time upper thermospheric winds over Millstone Hill between 1984 and 1990. *Journal of Geophysical Research*, 98(A3), 3731–3739. <https://doi.org/10.1029/92JA01605>

Harding, B. J., Gehrels, T. W., & Makela, J. J. (2014). Nonlinear regression method for estimating neutral wind and temperature from Fabry-Perot interferometer data. *Applied Optics*, 53, 666–673. <https://doi.org/10.1364/AO.53.000666>

Hedin, A. E. (1991). Extension of the MSIS thermosphere model into the middle and lower atmosphere. *Journal of Geophysical Research*, 96(A2), 1159–1172. <https://doi.org/10.1029/90JA02125>

Hedin, A. E., Fleming, E. L., Manson, A. H., Schmidlin, F. J., Avery, S. K., Clark, R. R., et al. (1996). Empirical wind model for the upper, middle and lower atmosphere. *Journal of Atmospheric and Terrestrial Physics*, 58(13), 1421–1447. [https://doi.org/10.1016/0021-9169\(95\)00122-0](https://doi.org/10.1016/0021-9169(95)00122-0)

Hedin, A. E., Buonsanto, M. J., Codrescu, M., Duboin, M.-L., Fesen, C. G., Hagan, M. E., & Sippler, D. P. (1994). Solar activity variations in midlatitude thermospheric meridional winds. *Journal of Geophysical Research*, 99(A9), 17,601. <https://doi.org/10.1029/94JA01134>

Hedin, A. E., & Spencer, T. L. (1988). Empirical global model of upper thermosphere winds based on atmosphere and dynamics explorer satellite data. *Journal of Geophysical Research*, 93(A9), 9959. <https://doi.org/10.1029/JA093iA09p09959>

Hernandez, G., & Roble, R. G. (1984). The geomagnetic quiet nighttime thermospheric wind pattern over Fritz Peak Observatory during solar minimum and maximum. *Journal of Geophysical Research*, 89(A1), 327–337. <https://doi.org/10.1029/JA089ia01p00327>

Hernandez, G., & Roble, R. G. (1995). Thermospheric nighttime neutral temperature and winds over fritz peak observatory: Observed and calculated solar cycle variation. *Journal of Geophysical Research*, 100(A8), 14,647–14,660. <https://doi.org/10.1029/95JA00565>

Hernandez, G., Roble, R. G., & Allen, J. H. (1980). Midlatitude thermospheric winds and their relationship to the auroral electrojet activity index. *Geophysical Research Letters*, 7, 677–680. <https://doi.org/10.1029/GL007i009p00677>

Hutchinson, J. A., Wright, S. E., & Grocott, A. (2011). A superposed epoch analysis of geomagnetic storms over a solar cycle. In *42nd Lunar and Planetary Science Conference*.

Kaab, M., Benkhaldoun, Z., Fisher, D. J., Harding, B., Bounhir, A., Makela, J. J., et al. (2017). Climatology of thermospheric neutral winds over Oukameden Observatory in Morocco. *Annales Geophysicae*, 35(1), 161–170. <https://doi.org/10.5194/angeo-35-161-2017>

Kawamura, S., Otsuka, Y., Zhang, S.-R., Fukao, S., & Oliver, W. L. (2000). A climatology of middle and upper atmosphere radar observations of thermospheric winds. *Journal of Geophysical Research*, 105(A6), 12,777–12,788. <https://doi.org/10.1029/2000JA900013>

Klobuchar, J. A. (1996). Ionospheric effects on GPS, global positioning system: Theory and applications. *American Institute of Aeronautics & Astronautics*, 1, 485–515.

Knipp, D. J., Tobiska, W. K., & Emery, B. A. (2004). Direct and indirect thermospheric heating sources for solar cycles 21–23. *Solar Physics*, 224, 495–505.

Lee, C.-C., Liu, J.-Y., Reinisch, B. W., Lee, Y.-P., & Liu, L. (2002). The propagation of traveling atmospheric disturbances observed during the April 6–7, 2000 ionospheric storm. *Geophysical Research Letters*, 29(5), 1068. <https://doi.org/10.1029/2001GL013516>

Lee, C.-C., Liu, M.-Q. S. S.-Y., Yeh, H.-C., & Nozaki, K. (2004). Observation and model comparisons of the traveling atmospheric disturbances over the Western Pacific region during the 6–7 April 2000 magnetic storm. *Journal of Geophysical Research*, 109, A09309. <https://doi.org/10.1029/2003JA010267>

Link, R., & Cogger, L. (1988). A reexamination of the OI 6300-Å nightglow. *Journal of Geophysical Research*, 93, 9883–9892. <https://doi.org/10.1029/JA093iA09p09883>

Liu, L. (2004). Solar activity variations of equivalent winds derived from global ionosonde data. *Journal of Geophysical Research*, 109, A12305. <https://doi.org/10.1029/2004JA010574>

Liu, H., Watanabe, S., & Kondo, T. (2009). Fast thermospheric wind jet at the Earth's dip equator. *Geophysical Research Letters*, 36, L08103. <https://doi.org/10.1029/2009GL037377>

Makela, J. J., Meriwether, J. W., Lima, J. P., Miller, E. S., & Armstrong, S. J. (2009). The remote equatorial nighttime observatory of ionospheric regions project and the international heliospherical year. *Earth, Moon, and Planets*, 104, 211–226. <https://doi.org/10.1007/s11038-008-9289-0>

Malki, K., Bounhir, A., Benkhaldoun, Z., Makela, J. J., Vilmer, N., Fisher, D. J., et al. (2018). Ionospheric and thermospheric response to the 27–28 February 2014 geomagnetic storm over North Africa. *Annales Geophysicae*, 36(4), 987–998. <https://doi.org/10.5194/angeo-36-987-2018>

Meriwether, J. W. (2008). Thermospheric dynamics at low and mid-latitudes during magnetic storm activity. *Geophysical Monograph Series*.

Nadia, I., Y., W., & K., M. (2019). Response of low to midlatitude ionosphere to the geomagnetic storm of September 2017. *Annales Geophysicae*, 38, 359. <https://doi.org/10.5194/angeo-2019-19>

Oliveira, D. M., Zesta, E., Schuck, P. W., & Sutton, E. K. (2017). Thermosphere global time response to geomagnetic storms caused by coronal mass ejections. *Journal of Geophysical Research: Space Physics*, 122, 10,762–10,782. <https://doi.org/10.1002/2017JA024006>

Roble, R. G., Ridley, E. C., Richmond, A. D., & Dickinson, R. E. (1988). A coupled thermosphere/ionosphere general circulation model. *Geophysical Research Letters*, 15(12), 1325–1328. <https://doi.org/10.1029/GL015i012p01325>

Sardon, E., Rius, A., & Zarraoa, N. (1994). Estimation of the transmitter and receiver differential biases and the ionospheric total electron content from global positioning system observations. *Radio Science*, 29, 577–586. <https://doi.org/10.1029/94RS00449>

Schaer, S. (1999). Mapping and predicting the Earth's ionosphere using the global positioning system. *Geod.-Geophys. Arb. Schweiz*, Zrich, Switzerland, 59.

Sean, L., Bruinsma, & Forbes, J. M. (2007). Global observation of traveling atmospheric disturbances (TADs) in the thermosphere. *Geophysical Research Letters*, 34, L14103. <https://doi.org/10.1029/2007GL030243>

Sethi, V. M.-K., Pandey, V. K., & Mahajan, K. K. (2001). Comparative study of TEC with IRI model for solar minimum period at low latitude. *Advances in Space Research*, 27, 45–48. [https://doi.org/10.1016/s0273-1177\(00\)00139-3](https://doi.org/10.1016/s0273-1177(00)00139-3)

van de Heyde, V. P. (2012). An investigation of magnetic storm effects on total electron content over South Africa for selected periods in solar cycles 23 and 24. A thesis submitted in partial fulfillment of the requirements of the degree of Magister Scientiae in the Department of Physics, University of the Western Cape.

Walker, G. O. (1973). Observations of ionospheric storms at low latitudes and their correlation with magnetic field changes near the magnetic equator. *Journal of Atmospheric and Terrestrial Physics*, 35, 1573–1582. [https://doi.org/10.1016/0021-9169\(73\)90176-1](https://doi.org/10.1016/0021-9169(73)90176-1)

Wang, W., Burns, A. G., M. Wiltberger, S. C. S., & Killeen, T. L. (2004). Altitude variations of the horizontal thermospheric winds during geomagnetic storms. *Journal of Geophysical Research*, 113, A02301. <https://doi.org/10.1029/2007JA012374>

Xiong, X.-P., Vogler, G., Kurthkoti, K., Samsonova, A., & Zhou, R. (2015). SmD1 modulates the miRNA pathway independently of its Pre-mRNA splicing function. *PLOS Genetics*, 11(8), e1005475. <https://doi.org/10.1371/journal.pgen.1005475>

Yagi, T., & Dyson, P. L. (1985). The response of the mid-latitude thermospheric wind to magnetic activity. *Planetary and Space Science*, 33, 461–467. [https://doi.org/10.1016/0032-0633\(85\)90090-x](https://doi.org/10.1016/0032-0633(85)90090-x)

Yokoyama, N., & Kamide, Y. (1997). Statistical nature of geomagnetic storms. *Journal of Geophysical Research*, 102(A7), 14,215–14,222. <https://doi.org/10.1029/97JA00903>

Zoundi, C., Ouattara, F., Fleury, A.-M. C., & Lassudrie-Duchesne, P. (2012). Seasonal TEC variability in west africa equatorial anomaly region. *European Journal of Scientific Research*, 77, 309–319.